DNA-guided lattice remodeling of carbon nanotubes

Zhiwei Lin[1*], Leti Beltran[2], Zeus A. De los Santos[1], Yinong Li[3], Tehseen Adel[4], Jeffrey A Fagan[1], Angela R. Hight Walker[4], Edward H. Egelman[2], and Ming Zheng[1*]

[1]Materials Science and Engineering Division, National Institute of Standards and Technology, Gaithersburg, MD 20899, USA
[2]Department of Biochemistry and Molecular Genetics, University of Virginia, Charlottesville, VA 22908, USA
[3]South China Advanced Institute for Soft Matter Science and Technology, School of Emergent Soft Matter, South China University of Technology, Guangzhou 510640, China
[4]Quantum Metrology Division, National Institute of Standards and Technology, Gaithersburg, MD 20899, USA

* zhiweilin@scut.edu.cn (ORCID ID: 0000-0001-9194-1145), ming.zheng@nist.gov (ORCID ID: 0000-0002-8058-1348)

One-Sentence Summary: A DNA-guided synthetic pathway leading to lattice remodeling of carbon nanotubes is discovered.

Abstract: Covalent modification of carbon nanotubes is a promising strategy to engineer their electronic structures. However, keeping modification sites in registration with a nanotube lattice is challenging. We report here a solution using DNA-directed, guanine (G)-specific crosslinking chemistry. By DNA screening we identify a sequence $C_3GC_7GC_3$ whose reaction with an (8,3) enantiomer yields minimum disorder-induced Raman mode intensities and photoluminescence Stokes shift, suggesting ordered defect array formation. Single-particle cryo-EM shows that the $C_3GC_7GC_3$ functionalized (8,3) has an ordered helical structure with a 6.5Å periodicity. Reaction mechanism analysis suggests that the helical periodicity arises from an array of G-modified carbon-carbon bonds separated by a fixed distance along an armchair helical line. Our findings may be used to remodel nanotube lattices for novel electronic properties.

Keywords: supramolecular chemistry, organic quantum material, carbon nanotube, DNA, cryo-EM

Synthesis of carbon-based quantum materials can in principle employ rich organic chemistry to realize novel properties via atomic-precision structural engineering. Over 50 years ago, W. A. Little proposed a room-temperature organic superconductor model composed of a one-dimensional conducting chain with an array of polarizable side chains attached (*1*). In the ensuring years, numerous efforts had been made but failed to verify Little's proposal (*2*). In 2016, the mechanism underlying Little's model –electron attraction mediated by polarizable groups– was confirmed for the first time (*3*). The study used a single-wall carbon nanotube (SWCNT) as the

one-dimensional conducting chain, along which a nanotube circuitry was constructed to provide a single polarizable "side chain". This work suggests a route to the Little model by chemically implanting polarizable groups in registration with a SWCNT lattice, but the task is deemed formidable (*4*). A major challenge is to control reaction sites along the nanotube, which seems insurmountable because half population of carbon atoms on a SWCNT are chemically equivalent and are enantiomers of the remaining half. Here we report a DNA-guided chemical reaction to overcome the challenge. We screen reaction products by resonance Raman and photoluminescence (PL) spectroscopy, and inspect the structures of promising candidates by single-particle cryo-EM. Our findings demonstrate feasibility to create a wide range of SWCNT derivatives in general, and to build a Little model in particular.

Broadly speaking, covalent modification of SWCNTs is a promising route towards organic quantum materials (*5-7*). With all atoms on their surfaces, SWCNTs are more amenable than other solid-state materials to precision molecular engineering by wet chemistry. In addition, various chiral forms of SWCNTs made available by sorting (*8*) offer a diverse range of electronic structures for further chemical tailoring. Recently, Weisman *et al.* reported a photochemical reaction of DNA-wrapped SWCNTs with singlet oxygen that covalently links guanine (G) to the side wall of SWCNTs (*6*). Even though the chemical nature of the covalent link was not fully revealed, and the structure of the reaction product rather disordered (*9*), we are nevertheless inspired to pursue ordered SWCNT lattice modification with the idea of finding more effective ways to explore the nanotube chirality and DNA sequence space.

To speed up sequence screening and to promote ordered structure formation, we have explored conditions for the guanine functionalization reaction of SWCNTs. We find that the previously reported aqueous phase photochemical reaction of Rose Bengal (RB) mediated guanine crosslinking with SWCNTs (*6*) also works in methanol/water mixed solvents. In 50 % v/v methanol, the reaction proceeds slower than that in water (reaction time 60 min *versus* 15 min in water); consumption of RB sensitizer is decreased dramatically; and RB binding to SWCNTs, which may adversely affect DNA wrapping structure and crosslinking site, is also minimized. All these changes should favor homogeneous product formation. Combining this new reaction condition with a previously established process (*10*) for DNA/surfactant exchange, we have devised a one-pot chemistry (**Fig. 1A, Figs. S1-5**) that can efficiently react any G-containing sequence with any single-chirality SWCNT species [*e.g.*, (6,5), (9,1), (8,3), *etc*..] purified independently via various techniques (*8*). Excess DNA is present during the reaction in order to refill exposed nanotube surfaces arising from reaction-induced DNA structure contraction, eliminating a potential source of inhomogeneous functionalization.

We have employed spectroscopic tools to monitor the reaction (**Fig. 1, Figs. S6-7**). **Figs. 1B-D** present a data set from a reaction on an (8,3) enantiomer (normalized circular dichroism signal at the E_{22} = – 42 mdeg, which according to theoretical analysis corresponds to a right-handed enantiomer(*11*)). Hereafter we denote the enantiomer simply as (8,3) unless indicated otherwise. **Figs. 1B** and **1C** show, respectively, the expected red-shift of the E_{11} absorption and PL peak after functionalization. **Fig. 1D** shows resonance Raman spectra of unfunctionalized (black trace) and functionalized (8,3) (red trace). In addition to the well-documented D peak, we find another

disorder-induced peak: the intermediate frequency mode (IFM)(*12, 13*) at 387 cm^{-1}, its overtone 2 IFM at 775 cm^{-1}, and its combination modes with D: D ± IFM at 905 and 1680 cm^{-1}, respectively. There is a dramatic intensity enhancement of the D and IFM modes in functionalized tubes. In contrast, 2IFM and D ± IFM peaks remain weak and unchanged after functionalization, consistent with their origin from two-phonon, second-order scattering processes (*12*).

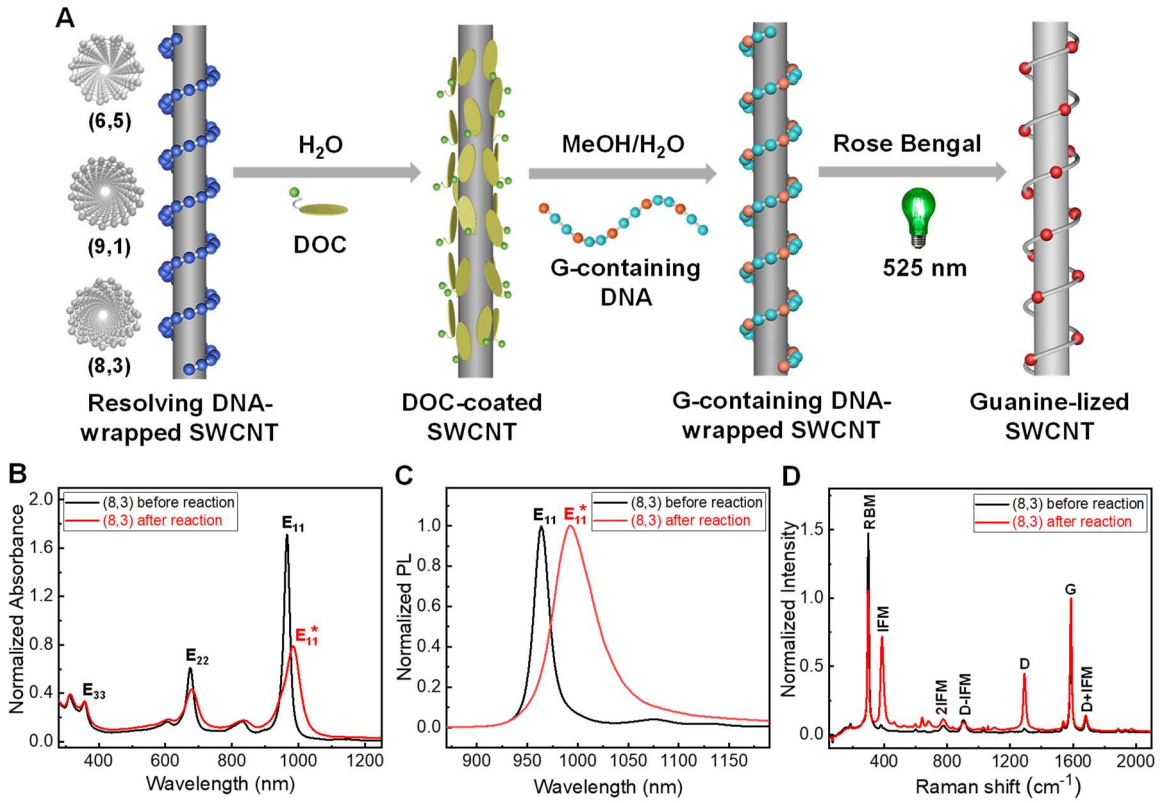

Fig. 1. One-pot photochemical reaction scheme and spectral characterization. (A) Reaction scheme starting from resolving DNA-wrapped to guanine-functionalized (guanine-lized) SWCNT carried out in a single pot; **(B)** Absorption (normalized at E_{33}); **(C)** PL (with peak intensity normalized to 1); and **(D)** Resonance Raman spectra (normalized at the "G" peak) of (8,3) before and after reaction. Spectra in **C** and **D** are measured with 671 nm excitation corresponding to E_{22} of (8,3). The DNA sequence used in this experiment is $(GCC)_{12}$. Also see **Fig. S8** for data shown in **B** and **C** before normalization.

To gain insight into the reaction mechanism, we have functionalized (8,3) using a set of DNA sequences with varying G content. With increasing G content, the functionalized (8,3) shows a gradual increase in both D and IFM peak intensity (**Figs. 2A** and **2B**), and more red-shifted and broadened PL and absorbance peaks (**Figs. 2C and 2D**). These observations are consistent with the previous study using mixed chirality tubes (*6*). However, using chirality-pure SWCNTs allows us to determine unambiguously the absorption and PL peak positions of the functionalized tube, and calculate its absorption peak shift and Stokes shift *SS*, *i.e.*, the energy difference between the

absorption and PL peak, as a function of G content or defect density. The absorption peak shift increases with G content (**Fig. 2E**), but its amplitude is less than 27 meV, about 10 times smaller than that typically observed for an sp^3 defect (*14*). This difference is striking considering that the defect density ($\approx 10^0$/nm) in guanine modified tubes (*15*) is about two orders of magnitude higher than that in sp^3 modified tubes (*5*). The *SS* also increases with defect density (**Fig. 2E**) – a trend opposite to that observed for sp^3 defect (*14*). In addition, we find a quantitative relationship between *SS* and full width at half maximum (FWHM = *W*) of the PL peaks, suggesting that modified and unmodified carbon atoms are isovalent as reasoned below. In **Fig. 2F**, we plot *SS vs* W^2 and fit the data well (R^2 = 0.98) with *T* = 349.3K using eq. (1), where *k* is the Boltzmann constant and *T* is the effective exciton temperature equal to or above the ambient temperature.

$$SS = \frac{W^2}{8 \ln 2 \; kT} \cong 0.18 \frac{W^2}{kT} \qquad (1)$$

Eq. (1) has been used to describe excitons in 2D quantum wells and 3D alloy semiconductors where disordered isovalent substitution creates shallow traps (*16, 17*). It attributes the observed *SS* to the thermalization of excitons in an inhomogeneously broadened band. Combining all of these spectroscopic observations, we exclude sp^3 defect formation by guanine functionalization and conclude that the chemistry creates a modified sp^2 defect that is isovalent to the original sp^2 carbon in the pristine SWCNT.

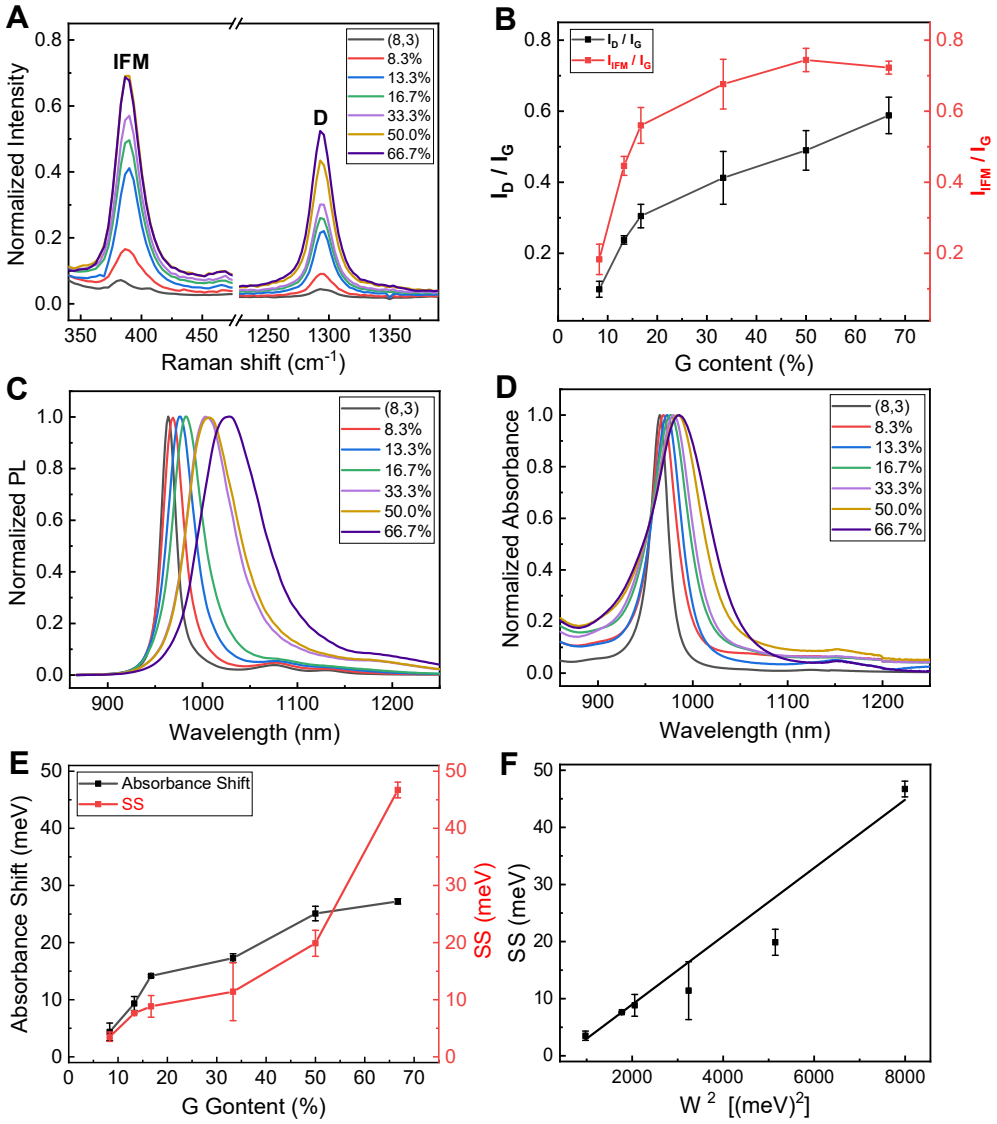

Fig. 2. Spectroscopic characterization of (8,3) functionalized with DNA of varying G content (see **Table S1** for sequence information)**. (A)** and **(B)** IFM and D peak intensity (normalized by the intensity of the "G" peak) profile; **(C) and (D)** PL and absorbance profile; **(E)** Absorbance shift and *SS* profile; **(F)** *SS* vs W^2 and a linear fit ($R^2 = 0.98$) using eq. (1) with $T = 349.3$K. Error bar shown here and elsewhere in this work represents standard deviation derived from three independently measured values for each of three independently prepared samples. Spectra in **A**, **C** and **D** are measured with 671 nm excitation. Also see **Fig. S9** for original data.

To differentiate two types of disorder originating from the defect density itself and defect distribution pattern, we have designed a set of 15-mer G/C sequences containing two Gs separated by a varying number of Cs (**Fig. 3A**) for the (8,3) functionalization chemistry. We find that disorder-induced D and IFM peak intensities change as a function of the inter-G spacing, reaching

a surprisingly deep minimum when the spacing is 7 (**Figs. 3B** and **3C**). The *SS* and PL peak linewidth also show minimum values at that spacing (**Figs. 3D** and **3E**). These observations appear to be dependent on nanotube chirality, since left- and right-handed (6,5)s functionalized by the same set of sequences yield different spectral patterns (**Fig. S7**).

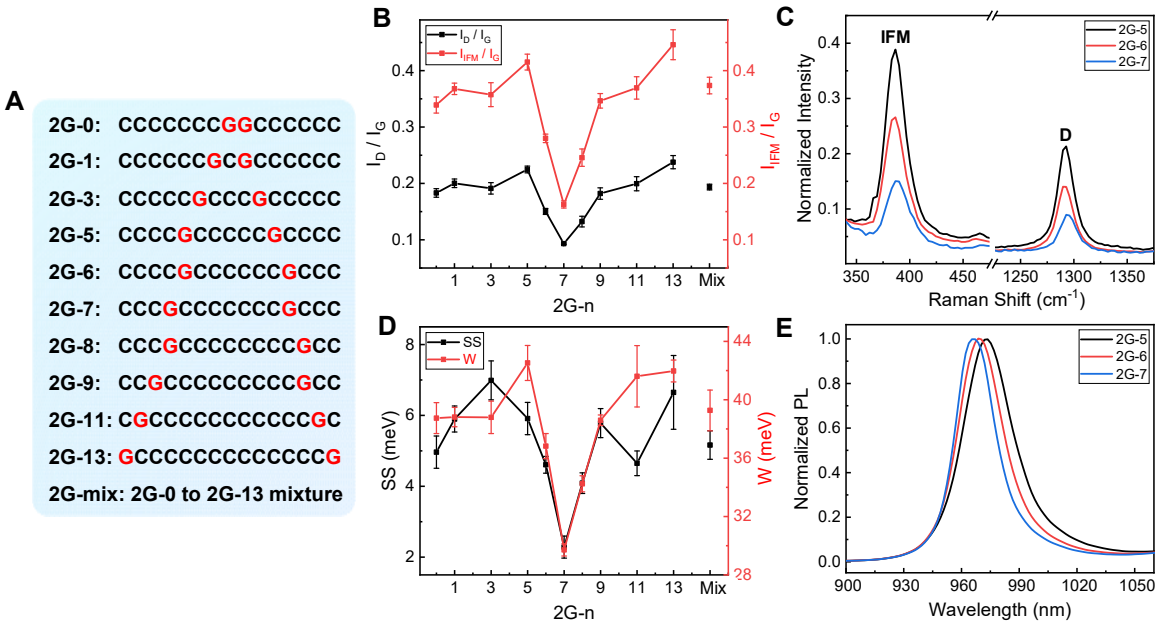

Fig. 3. Screening DNA sequences for ordered defect array. (A) DNA sequence used for the screening; **(B)** D and IFM peak intensity profile; **(C)** Raman spectra of 2G-5, 2G-6, and 2G-7 functionalized (8,3) (normalized by the "G" peak); **(D)** *SS* and *W* profile; **(E)** PL spectra of the three samples. Spectra in **C** and **E** are measured with 671 nm excitation. Also see **Fig. S10** for original data.

We offer a qualitative analysis of the data shown in **Fig. 3**. According to the mechanism of defect-induced Raman modes (*12, 18*), the observed peak intensity is proportional to the extent of elastic electron scattering by defects. For sequences used in our study, we estimate that a SWCNT contains 1-5 guanine modified sites per nm tube length based on molecular dynamics simulations of a typical DNA wrapping structure on a SWCNT (*15*). Because the size of excitons is 2 to 3 nm (*19*), electron scattering is expected to involve multiple defect sites, and is sensitive to not only the defect density but also the degree of order of the defect array. The minimum D and IFM peak intensities shown in **Fig. 3** are thus interpreted as resulting from an ordered defect array generated by the 2G-7 sequence. This conclusion is also consistent with the observed minimum *SS* for the same sequence, as *SS* is another measure of disorder for semiconductors with isovalent substitution (*16, 17*).

To independently evaluate the spectroscopy-derived result, we have applied single-particle cryo-EM to measure 2G-7-(8,3) hybrid structure before and after functionalization. Cryo-EM imaging of 2G-7 functionalized (8,3) reveals filaments of approximately 20Å in diameter (**Fig. S11**). In the non-functionalized structure coated with 2G-7, an averaged power spectrum from ≈

2×10^5 images of particle segments yields no detectable features (**Fig. S12**), implying a disordered DNA wrapping structure. In the functionalized structure, we have detected a layer line pattern characteristic of a 1-start helix with 6.5 Å helical pitch visible from the averaged power spectrum of selected segments (**Fig. 4A**). The helical structure is also visible in the two-dimensional (2D) class average (**Fig. 4B**). *Ab initio* reconstruction, an unbiased and reference free approach, was employed to generate a 3D reconstruction of the DNA coated nanotube (**Fig. 4C**). **Fig. 4D** shows a highly averaged version of that reconstruction, with an atomic model for the SWCNT. Due to the low signal-to-noise ratio in these cryo-EM images, and the apparent lack of any other periodicities present, we have imposed a helical averaging of the density along the 6.5 Å pitch helix. The unfiltered 3D map (**Fig. 4C**) shows a coherence length that is about 10 nm long, shorter than the full length of the segments used. The density in **Figs. 4C** and **4D** is shown as a left-handed helix, however, true handedness was not determined.

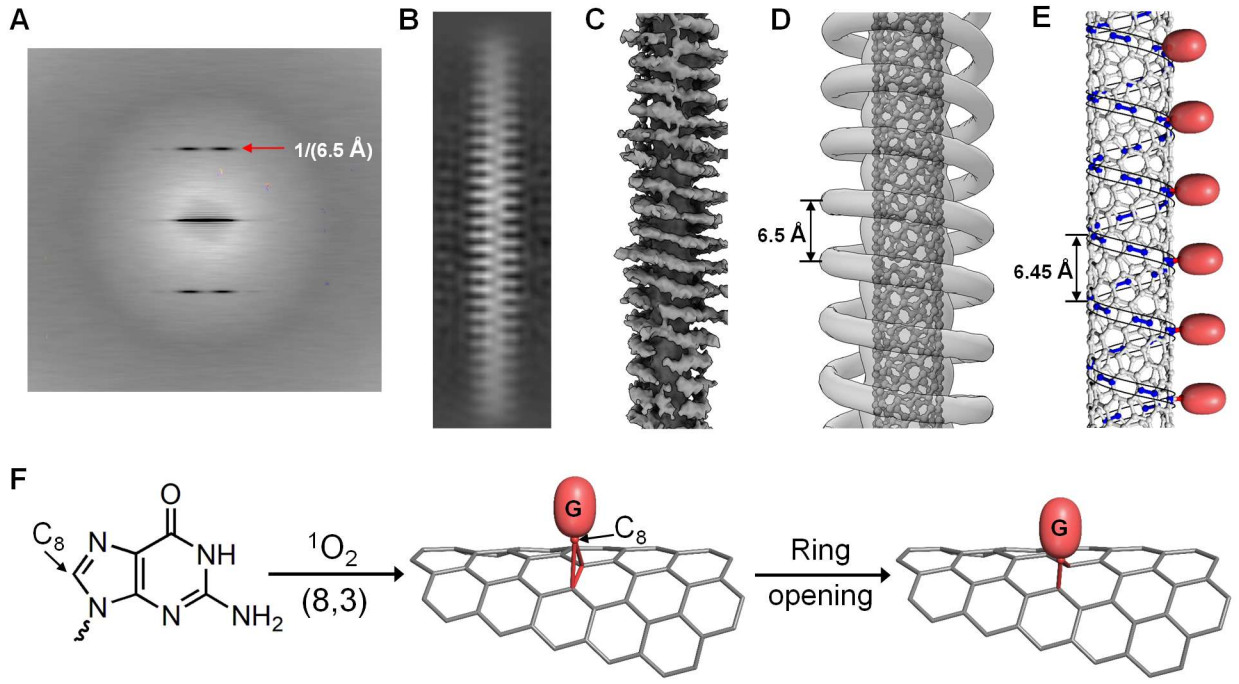

Fig. 4. Cryo-EM derived structure model for 2G-7 functionalized (8,3) and reaction mechanism. (A) Averaged power spectrum from approximately 44000 particles. Red arrow points to a layer line with a spacing of 1/(6.5 Å) from the equator; **(B)** Image of 2D class average; **(C)** Low-resolution 3D map generated by unbiased, reference-free approach displays coherence that extends over an axial length of ≈ 10 nm; **(D)** 3D map corresponding to averaged density along the 6.5 Å pitch helix; **(E)** Carbon-carbon bonds that have maximum bond curvature, highlighted in blue along an armchair helical line of (8,3), along which every sixth carbon-carbon bond is modified by a guanine (red balls) according to modeling (**Fig. S14A**); **(F)** A proposed reaction mechanism.

The 6.5 Å periodicity observed by cryo-EM provides support for the model of ordered defect array formation and an important clue to the mechanism of guanine functionalization. As discussed

earlier, a correct reaction mechanism should yield a modified carbon that largely maintains its sp^2 character. Indeed, such chemistry has been well-documented (*20, 21*) and forms the basis for our proposal shown in **Figs. 4E, 4F, and S14B**. Guanine oxidation by singlet oxygen has a plethora of pathways and products depending on reaction conditions and structural context, but a common initial step is oxidation of the C_8 carbon on the imidazole ring (*22*). We propose that the C_8 carbon becomes electrophilic upon oxidation, and then undergoes a 2+1 cycloaddition with a nearby C-C bond on a SWCNT to yield a three-membered ring. This is followed by the C-C bond cleavage and concomitant ring opening due to ring strain, leaving C_8 to bridge the two carbons from the SWCNT and restore their sp^2 character. Theoretical calculation (*20*) predicts that this type of reaction is most favorable on C-C bonds with large curvature or bond strain, consistent with a previous observation from the guanine functionalization chemistry (Figure 2C in reference (*6*)). In (8,3), there are three types of C-C bonds with distinct curvatures. C-C bonds along a helical armchair line shown in **Fig. 4E** possess the largest curvature. We note that the pitch p of this helical line is an intrinsic length scale of (8,3) determined solely by its chiral index *(n, m)* and C-C bond length a_c: $p = a_c\sqrt{n^2+m^2+nm}\,\frac{n-m}{n+m} = 6.45$ Å $(for\ a_c = 1.44$ Å$)$, matching that observed by the cryo-EM. We therefore propose a 2G-7 wrapping structure where each of the 2Gs is covalently linked to a C-C bond along the armchair line, resulting in pinning of the DNA backbone along the same armchair line. Consistent with this functionalization-induced DNA pinning is our observation that 2G-5 and 2G-6 functionalized (8,3) also exhibit the same 6.5 Å helical pitch (**Fig. S13**). Manual model building for 2G-7 functionalized (8,3) followed by energy minimization yields a model shown in **Fig. S14A**, in which two adjacent G modification sites are separated by 5 C-C bonds along the armchair line. This equal G spacing explains minimum spectroscopy-derived structure disorder for 2G-7 functionalized (8,3).

In summary, we show that ordered SWCNT modification can be achieved by taking advantage of DNA sequence control over the spacing between adjacent reaction sites, and SWCNT's bond curvature dependent reactivity. Our finding demonstrates chemical feasibility to build a Little model. DNA-guided remodeling breaks the original symmetry of the nanotube lattice, and therefore should lead to new modes of low-energy electronic excitation. Theoretical analysis shows that helical modification of a SWCNT in registry with its lattice may induce topological electronic behavior (*23, 24*), suggesting that the chemistry we report here might be used to explore topological physics. We envision that future work will introduce diversity of functional groups, increase the coherent length of ordered modification, and eventually enable discovery of organic quantum materials and carbon-based metal-free catalysts (*25, 26*).

Supplementary materials: Materials and methods, **Figs. S1-S14**, and references (*27-30*).

Acknowledgements

We thank Bruce Weisman and Sergei Tretiak for useful discussion. **Funding:** supported by NIST internal funding and NIH GM122510 (to E. H. E.). Z. A. D. acknowledges NRC postdoctoral

fellowship. **Author contributions**: Z. L. and M. Z. conceived the idea. Z. L. and Z. A. D. performed experiments, J. A. F. provided samples, L. B. and E. H. E. performed cryo-EM and analysis, Z. L. and Y. L. performed molecular modeling, T. A. and A. R. H. W. performed Raman analysis, Z. L., M. Z., L. B., and E. H. E. wrote the manuscript with input from all authors. **Competing interests:** None declared. **Data and materials availability:** All data needed to evaluate the conclusions in the paper are present in the paper or the Supplementary Materials.

References and Notes

1. W. A. Little, Possibility of Synthesizing an Organic Superconductor. *Physical Review* **134**, A1416-A1424 (1964).
2. D. Jérome, The Physics of Organic Superconductors. *Science* **252**, 1509-1514 (1991).
3. A. Hamo *et al.*, Electron attraction mediated by Coulomb repulsion. *Nature* **535**, 395-400 (2016).
4. T. Kontos, Attractive electrons from nanoengineering. *Nature* **535**, 362-363 (2016).
5. Y. Piao *et al.*, Brightening of carbon nanotube photoluminescence through the incorporation of sp3 defects. *Nature Chemistry* **5**, 840-845 (2013).
6. Y. Zheng, S. M. Bachilo, R. B. Weisman, Controlled Patterning of Carbon Nanotube Energy Levels by Covalent DNA Functionalization. *ACS Nano* **13**, 8222-8228 (2019).
7. F. Yang *et al.*, Chirality Pure Carbon Nanotubes: Growth, Sorting, and Characterization. *Chemical Reviews* **120**, 2693-2758 (2020).
8. M. Zheng, Sorting Carbon Nanotubes. *Topics in Current Chemistry* **375**, 13 (2017).
9. Y. Zheng *et al.*, Quantum Light Emission from Coupled Defect States in DNA-Functionalized Carbon Nanotubes. *ACS Nano* **15**, 10406-10414 (2021).
10. J. K. Streit, J. A. Fagan, M. Zheng, A Low Energy Route to DNA-Wrapped Carbon Nanotubes via Replacement of Bile Salt Surfactants. *Analytical Chemistry* **89**, 10496-10503 (2017).
11. N. Sato, Y. Tatsumi, R. Saito, Circular dichroism of single-wall carbon nanotubes. *Physical Review B* **95**, 155436 (2017).
12. A. Vierck, F. Gannott, M. Schweiger, J. Zaumseil, J. Maultzsch, ZA-derived phonons in the Raman spectra of single-walled carbon nanotubes. *Carbon* **117**, 360-366 (2017).
13. T. Inaba, Y. Tanaka, S. Konabe, Y. Homma, Effects of Chirality and Defect Density on the Intermediate Frequency Raman Modes of Individually Suspended Single-Walled Carbon Nanotubes. *The Journal of Physical Chemistry C* **122**, 9184-9190 (2018).
14. F. J. Berger *et al.*, Brightening of Long, Polymer-Wrapped Carbon Nanotubes by sp3 Functionalization in Organic Solvents. *ACS Nano* **13**, 9259-9269 (2019).
15. D. Roxbury, A. Jagota, J. Mittal, Structural Characteristics of Oligomeric DNA Strands Adsorbed onto Single-Walled Carbon Nanotubes. *The Journal of Physical Chemistry B* **117**, 132-140 (2013).
16. M. Gurioli, A. Vinattieri, J. Martinez-Pastor, M. Colocci, Exciton thermalization in quantum-well structures. *Physical Review B* **50**, 11817-11826 (1994).
17. M. Felici *et al.*, Compositional disorder in GaAs1-xNx:H investigated by photoluminescence. *Physical Review B* **74**, 085203 (2006).
18. C. Thomsen, S. Reich, Double Resonant Raman Scattering in Graphite. *Physical Review Letters* **85**, 5214-5217 (2000).
19. L. Lüer *et al.*, Size and mobility of excitons in (6, 5) carbon nanotubes. *Nature Physics* **5**, 54-58 (2009).
20. Y.-S. Lee, N. Marzari, Cycloaddition Functionalizations to Preserve or Control the Conductance of Carbon Nanotubes. *Physical Review Letters* **97**, 116801 (2006).
21. A. Setaro *et al.*, Preserving π-conjugation in covalently functionalized carbon nanotubes for optoelectronic applications. *Nature Communications* **8**, 14281 (2017).
22. Y. Ye *et al.*, Formation of 13C-, 15N-, and 18O-Labeled Guanidinohydantoin from Guanosine Oxidation with Singlet Oxygen. Implications for Structure and Mechanism. *Journal of the American Chemical Society* **125**, 13926-13927 (2003).
23. V. I. Puller, S. V. Rotkin, Helicity and broken symmetry of DNA-nanotube hybrids. *Europhysics Letters (EPL)* **77**, 27006 (2007).
24. C. Hu, V. Michaud-Rioux, W. Yao, H. Guo, Theoretical Design of Topological Heteronanotubes. *Nano Letters* **19**, 4146-4150 (2019).

25. K. Gong, F. Du, Z. Xia, M. Durstock, L. Dai, Nitrogen-Doped Carbon Nanotube Arrays with High Electrocatalytic Activity for Oxygen Reduction. *Science* **323**, 760-764 (2009).
26. X. Liu, L. Dai, Carbon-based metal-free catalysts. *Nature Reviews Materials* **1**, 16064 (2016).
27. G. Ao, C. Y. Khripin, M. Zheng, DNA-Controlled Partition of Carbon Nanotubes in Polymer Aqueous Two-Phase Systems. *Journal of the American Chemical Society* **136**, 10383-10392 (2014).
28. G. Ao, J. K. Streit, J. A. Fagan, M. Zheng, Differentiating Left- and Right-Handed Carbon Nanotubes by DNA. *Journal of the American Chemical Society* **138**, 16677-16685 (2016).
29. Z. A. De los Santos, Z. Lin, M. Zheng, Optical Detection of Stereoselective Interactions with DNA-Wrapped Single-Wall Carbon Nanotubes. *Journal of the American Chemical Society* **143**, 20628-20632 (2021).
30. M. Lyu, B. Meany, J. Yang, Y. Li, M. Zheng, Toward Complete Resolution of DNA/Carbon Nanotube Hybrids by Aqueous Two-Phase Systems. *Journal of the American Chemical Society* **141**, 20177-20186 (2019).

Supplementary Materials for

DNA-guided lattice remodeling of carbon nanotubes

Zhiwei Lin[1*], Leti Beltran[2], Zeus A. De los Santos[1], Yinong Li[3], Tehseen Adel[4], Jeffrey A Fagan[1], Angela R. Hight Walker[4], Edward H. Egelman[2], and Ming Zheng[1*]

[1]Materials Science and Engineering Division, National Institute of Standards and Technology, Gaithersburg, MD 20899, USA
[2]Department of Biochemistry and Molecular Genetics, University of Virginia, Charlottesville, VA 22908, USA
[3]South China Advanced Institute for Soft Matter Science and Technology, School of Emergent Soft Matter, South China University of Technology, Guangzhou 510640, China
[4]Quantum Metrology Division, National Institute of Standards and Technology, Gaithersburg, MD 20899, USA

* zhiweilin@scut.edu.cn; ming.zheng@nist.gov

Disclaimer: *Certain equipment, instruments or materials are identified in this paper in order to adequately specify the experimental details. Such identification does not imply recommendation by the National Institute of Standards and Technology (NIST), nor does it imply the materials are necessarily the best available for the purpose.*

This PDF file includes:

Materials and Methods
Table S1
Figs. S1 to S14
Full Reference List

Materials

CoMoCAT SWCNT powders (SG65i grade, lot no. L64) were obtained from Southwest Nanotechnologies. Oligomers of ssDNA were purchased from Integrated DNA Technologies. Polyethylene glycol (PEG, MW 1.5 kDa, Alfa Aesar), polyethylene glycol (PEG, MW 6 kDa, Alfa Aesar), dextran (DX, MW 250kDa, Alfa Aesar), polyvinylpyrrolidone (PVP, MW 10 kDa, Sigma-Aldrich), sodium phosphate dibasic (Na_2HPO_4, Sigma-Aldrich), sodium phosphate monobasic (NaH_2PO_4, Sigma-Aldrich), phosphoric acid (H_3PO_4, 85%, MCB Reagents), sodium thiocyanate (NaSCN, Sigma-Aldrich), sodium chloride (NaCl, BDH Chemicals), rose bengal (RB, dye content 95%, Sigma-Aldrich), phosphate buffer solution (NaPB, 1M, pH=7.4, Sigma-Aldrich), sodium deoxycholate (DOC, Sigma-Aldrich) were used as received.

UV-Vis-NIR absorption spectroscopy

UV-Vis-NIR absorption spectra were collected on a Cary 5000 spectrophotometer using a 1 cm path length quartz microcuvette. The volume for each analysis was typically 0.1 mL and all spectra were obtained with background subtraction.

PL and Raman spectroscopy

Photoluminescence (PL) and Raman spectra were collected using an NS3 Nanospectralyzer (Applied NanoFluorescence, Houston, TX) with two excitation wavelengths (532 and 671nm). The sample volume was typically 0.4 mL and all spectra were obtained at room temperature. Spectra were collected in presence of 0.25% DOC. The Raman $I_{D/IFM}/I_G$ ratio was calculated using peak intensities. We have also tried peak fitting followed by peak area integration to obtain intensities of defect- and G-peak and their ratio. These two methods yield similar results.

Purification of SWCNTs

DNA-SWCNT dispersions were prepared according to procedures reported previously (*27, 28*). Typically, SG65i-L64 SWCNT powders (1 mg) and ssDNA sequence (2.5 mg) are sonicated in either sodium phosphate buffer (30 mmol/L at pH = 4) for purification of GC_4G-(+)(6,5) and $(GCGCCC)_6$-(9,1), or sodium chloride (30 mmol/L) in aqueous solution for purification of $TTA(TAT)_2ATT$-(–)(6,5) and $T_3C_3T_3C_6$-(–)(8,3), giving 1 mg/mL of SWCNT-DNA dispersion.

$TTA(TAT)_2ATT$-(–)(6,5) and $T_3C_3T_3C_6$-(–)(8,3) were purified according to procedures reported previously (*29*). For the purification of GC_4G-(+)(6,5) and $(GCGCCC)_6$-(9,1), the following procedures were proceeded. Separate solutions of PEG 1.5 kDa and DX 250 kDa aqueous two-phase (ATP) stock solution (with two compositions 10:0 and 7:3) were prepared following the procedures identified in our previous publication (*30*). The mass fraction (%) of PEG 1.5kDa and DX 250kDa are 8.57 and 10.1 in 10:0 stock solution, and 12.2 and 14.4 in 7:3 stock solution, respectively. In a typical partition experiment, 3 volumes (120 μL) of SWCNT-DNA dispersion was loaded into 7 volumes (280 μL) of the 7:3 stock solution, giving a 10:0 ATP system at room temperature. In the first step, 2 μL 1% PVP (10 kDa) in water was added into the 10:0 ATP system. The mixture was vortexed and subsequently centrifuged and the first top fraction (1T) was extracted. 1T fraction containing either (+)(6,5) or (9,1) species was further incubated at 4 °C overnight, inducing a new two-phase separation. The new top fraction (1T-T) with a higher purity of (+)(6,5) or (9,1) species was collected and the SWCNT-DNA hybrids were precipitated by adding NaSCN to a final concentration of 0.5 mol/L. The supernatant liquid was completely removed. The pellets were resuspended in 20 mmol/L NaPB buffer (pH=7.4) to give pure SWCNT species with a concentration of OD ~20.

One-pot Chemistry

One-pot reaction to produce various functionalized DNA-SWCNTs were performed following a similar procedure. Here, we use 2G-7 ($C_3GC_7GC_3$)-functionalized (8,3) as an example to demonstrate a typical reaction. Into 10 μL $T_3C_3T_3C_6$-(8,3) with OD ~20, 6 μL NaPB buffer (20 mmol/L, pH=7.4), 2 μL 10% DOC and 6 μL 2G-7 (10 mg/mL) were added and vortexed. 105 μL MeOH was dropwise (5 μL/drop) added into the mixture under a vigorous vortexing condition. In this step, $T_3C_3T_3C_6$ are removed from (8,3) nanotubes, and 2G-7 are wrapped onto nanotubes, which is a process of DNA-DNA exchange. Then, 80 μL NaPB buffer (20 mmol/L, pH = 7.4) and 1 μL RB (6 mmol/L) was added into the mixture to reach a 50% v/v MeOH content. The entire reaction mixture contained in a 5 mL glass vial was stirred and illuminated by a pair of 525 nm LED lamps (PR160 Rig with Fan kit, Kessil) for 1 hour at room temperature. Note that the DNA-DNA exchange and the reaction take place in one-pot. With 50 times excess reacting DNA, replacement of the original wrapping DNA is estimated to be more than 98% complete. Any residue original wrapping DNA should be further replaced by the reactive G-containing sequences during the functionalization reaction. After reaction, the functionalized nanotubes were precipitated by adding NaSCN (5 mol/L) to a final concentration of 0.5 mol/L, and centrifuged at 17,000 G (G = 9.81 m/s^2) for 10 minutes. The supernatant liquid was completely removed. The pellets were resuspended in 20 mmol/L NaPB buffer (pH = 7.4) for further characterization. The unfunctionalized 2G-7 control sample used for cryo-EM characterization was prepared by following the above procedure without adding RB and going through the illumination.

Cryo-EM Sample Preparation and Data Collection

Sample containing either covalently linked 2G-5-, 2G-6-, 2G-7-(8,3) or unfunctionalized 2G-7-(8,3) carbon nanotubes at a concentration of OD ~5-10 was diluted 1:10 in distilled water, which has been passed through an ion exchange filtration system. In brief, a 2μL aliquot of sample was applied to a plasma-cleaned (Gatan Solarus) lacey carbon grids (Ted Pella, INC.), blotted with automated blotting for 3 s at 90% humidity and flash frozen in liquid ethane using an EM GP Plunge Freezer (Leica). The dataset used for structure determination was collected at the Molecular Electron Microscopy Core at the University of Virginia on a Titan Krios EM operated at 300 keV, equipped with an energy filter and K3 direct electron detector (Gatan). An energy filter slit width of 10 eV was used during data collection and was aligned automatically every hour. All 18,404 covalently linked 2G-7-(8,3) and 17,471 unfunctionalized 2G-7-(8,3) movies were collected in counting mode at a magnification of 105 K, pixel size of 0.86 Å. Data collection was performed using a total dose of 80 $e^- Å^{-2}$ across 60 frames at a rate of 4.80 s/movie.

Data Processing

Unless otherwise stated, all data processing was completed using cryoSPARC v3.2.0. Movies were corrected for full-frame motion using Patch Motion Correction followed by Gctf CTF Estimation. After CTF estimation, micrographs were sorted and selected based on estimated resolution (0 to 4Å), defocus (0.6 to -2.6 μm), ice thickness, and total full-frame motion. Initial particles were automatically picked using 'Filament Tracer' with a filament diameter of 100 Å and a separation distance of 0.1. Particles were extracted at a box size of 256 pixels, followed by 2D classification. Class averages containing filaments distinguishable from that of noise were selected for template-

based particle picking. A total of 29,453,362 particles were extracted using a box diameter of 260 Å. These particles were sorted using 2 iterative rounds of 2D classification with 50 classes each, number of online-EM iterations set to 20 and a batch size of 100 per class. The final iteration of 2D classification yielded a subset of 44,393 particles. Reconstructions of the 2G-7-(8,3) carbon nanotube was generated by two methods (1) an averaged power spectrum was generated using the raw images of aligned filament segments selected from 2D classification. A single layer line observed with a spacing of 6.5 Å from the meridian was used for helical averaging to produce a 3D map with all details smeared out, (2) an initial model was generated using an unbiased approach '*Ab-initio* reconstruction', class size set to 1. An output 3D map was inspected for structural motifs (i.e., ssDNA chain around a tube). Particles were further refined using iterations of homogeneous refinement with the input volume generated by single-class *ab initio*. A 3D map possessing low-resolution features was sharpened using a negative B-factor of 19.1.

The unfunctionalized 2G-7-(8,3) carbon nanotube movies were subjected to the same automated particle picking, sorting, and selecting protocol as the functionalized sample. A total of 11,873,739 particles were extracted using a box diameter of 256 Å and these particles were sorted using one round of 2D classification with 50 classes. Raw images of aligned filament segments, selected from 2D classification were used to generate an averaged power spectrum.

MD simulation

The GROMACS 2018.6 simulation package was used in conjunction with the CHARMM27 force field for MD simulation. The structure of (8,3) was created in VMD and the structure of $C_3GC_7GC_3$ (2G-7) was created in GROMACS. For the initial structure, three DNA strands of 2G-7 with the direction of 5'-3', 3'-5' and 5'-3' were sequentially placed around the (8,3), and the C_8 atom of guanine was covalently conjugated with a C-C bond on an armchair line. The functionalized 2G-7-(8,3) was solvated in a 50.0×50.0×83.7 Å water box. It contains around 6000 TIP3P model water molecules with the appropriate amount of sodium counterions to balance the negative phosphate charges. The final structure was obtained by energy minimization and annealing with a maximum temperature of 500 K. The final frame was visualized in VMD.

Table S1. DNA sequences of different G contents used in Fig. 2.

Sequence	G content (%)
GC_{11}	8.3
$GC_{13}G$	13.3
$(CCGCCC)_3$	16.7
$(GCCCCG)_3$	33.3
$(GCGCGC)_3$	50.0
$(GCCGGG)_3$	66.7

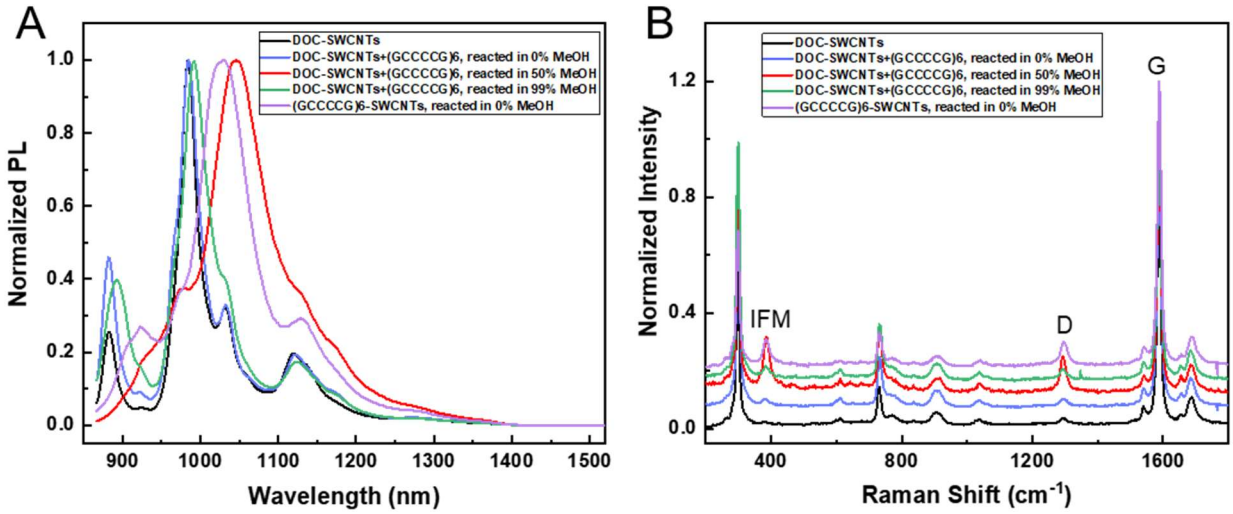

Fig. S1. (A) PL spectra and (B) Raman spectra of $(GCCCCG)_6$-functionalized SG65i SWCNTs under various conditions. **Black trace:** DOC-coated non-functionalized SWCNTs (serving as a control); **blue trace:** DOC-coated SWCNTs + $(GCCCCG)_6$, reacted in 0% MeOH; **red trace:** DOC-coated SWCNTs + $(GCCCCG)_6$, reacted in 50% MeOH; **green trace:** DOC-coated SWCNTs + $(GCCCCG)_6$, reacted in 99% MeOH; **purple trace:** $(GCCCCG)_6$-wrapped SWCNTs reacted in 0% MeOH.

Discussion on Fig. S1: To optimize the functionalization condition, we carried out the reaction between $(GCCCCG)_6$ and SG65i SWCNTs at 0%, 50% and 99% MeOH content, respectively. It is evident that no reaction occurs at 0% MeOH (blue trace), as DOC can't be replaced by G-containing DNA under this condition. On the other hand, at 99% MeOH the reaction is dramatically hindered due most likely to slowed singlet oxygen production (green trace). In contrast, 50% MeOH appears to be an optimal condition to enable both DOC/DNA exchange and singlet oxygen production. We also show in this experiment that reaction with DOC/DNA exchange at 50% MeOH results in more complete functionalization than that achieved with DNA-SWCNTs, which was prepared by direct sonication, as the starting material in aqueous solution (red trace *vs* purple trace in the figure).

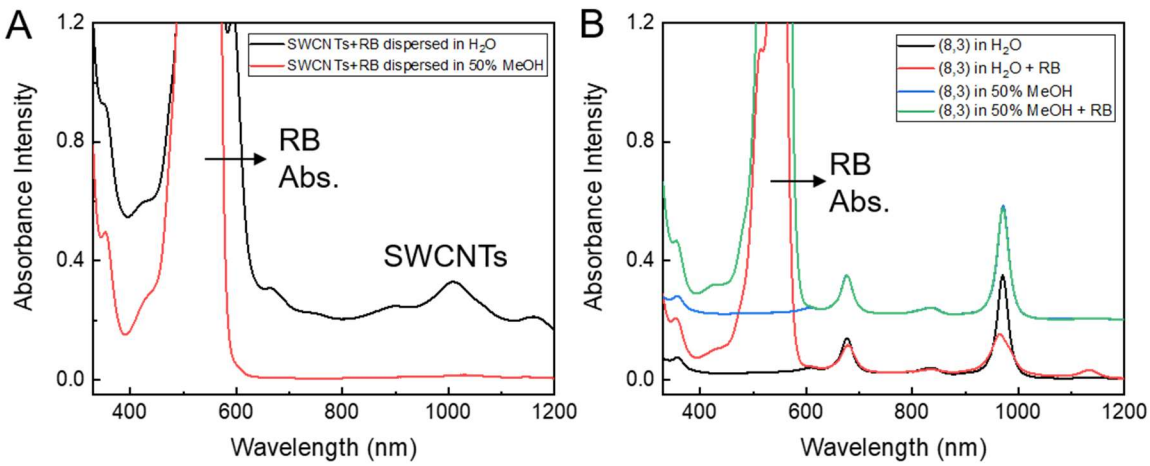

Fig. S2. (A) Absorbance spectra of rose Bengal (RB) dispersed SG65i-SWCNTs in water and 50% MeOH. (B) Absorbance spectra of GGCCGG-(8,3) in water and 50% MeOH, and in the absence and presence of 30 μM RB.

Discussion on Fig. S2: As an aromatic dye molecule, rose Bengal (RB) is expected to have binding affinity with SWCNTs via π-π stacking interaction. To clarify if RB interferes with DNA wrapping during the reaction (in 50% MeOH), a set of experiments were designed. (i) 1% (w/w) RB was used to disperse SWCNTs in water and 50% MeOH by sonication, respectively. As shown in **Fig. S2A**, 1% (w/w) RB can disperse SWCNTs in water, but not in 50% MeOH. This suggests that RB has much weaker binding affinity with SWCNTs in 50% MeOH than in water. (ii) Absorbance spectra of GGCCGG-(8,3) was measured in water and 50% MeOH with and without RB. As shown in **Fig. S2B**, addition of 30 μM RB to GGCCGG-(8,3) causes decreased E_{11} peak in water (black trace vs. red trace) but not in 50% MeOH (blue trace vs. green trace). It indicates that RB does not interfere with DNA in 50% MeOH. We thus conclude that MeOH minimize RB binding to SWCNTs and RB does not affect DNA conformation during the reaction.

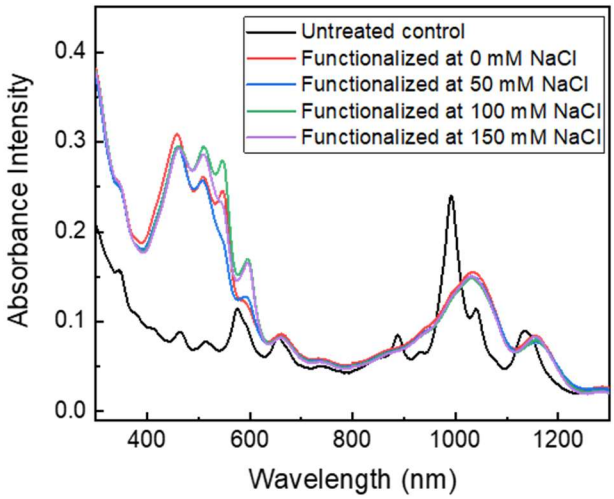

Fig. S3. Absorbance of functionalized SWCNTs at various salt concentrations. The reactive sequence used is GGGCGC.

Discussion on Fig. S3: Ionic strength could tune the stiffness of ssDNA and may exert influence on lattice modification of different (*n*, *m*) species. To directly test the effect of ionic strength, we conducted reactions at 0, 50, 100 and 150 mM NaCl (higher concentrations cause colloidal instability) to functionalize a (*n*, *m*) mixture (SG65i), which contains near-armchair (6,5), near-zigzag (9,1), and other chiralities in between. We reasoned that any (*n*, *m*)-dependent change in functionalization will cause spectral peak position and linewidth change. We therefore monitored reaction product by absorbance spectroscopy. **Fig. S3** shows the absorbance data, which indicates that RB consumption (absorption in the 400-600 nm) varies a little bit, but the absorption bands of functionalized SWCNTs in the 800 to 1300 nm region are insensitive to changes in salt concentration, implying that the profile of functionalized tubes remains constant.

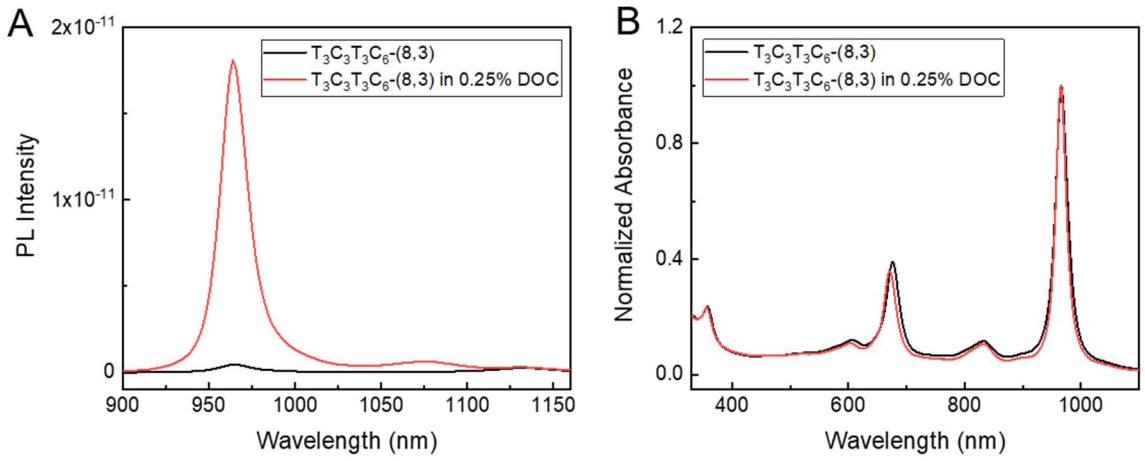

Fig. S4. (A) PL and (B) absorbance spectra of $T_3C_3T_3C_6$-(8,3) before and after adding 0.25% (w/w) DOC.

Discussion on Fig. S4: While DOC replacement of DNA is well-documented in the literature (*6*), to further illustrate the existence of DOC-coated SWCNTs in our case, we conducted experiments to monitor PL and absorbance change upon addition of DOC to $T_3C_3T_3C_6$-wrapped (8,3). As

shown in **Fig. S4**, addition of DOC causes a 40-fold PL increase and blue-shifted E_{11} and E_{22} absorbance peaks, indicating formation of new species.

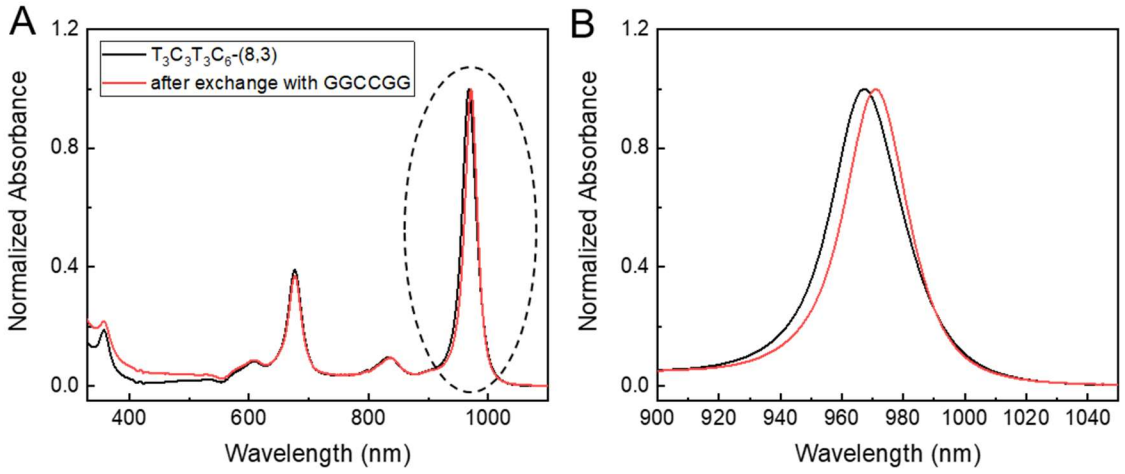

Fig. S5. (A) Absorbance spectra of $T_3C_3T_3C_6$-(8,3) before and after exchange with GGCCGG. (B) Zoomed-in view of E_{11} peak in panel A.

Discussion on Fig. S5: In the one-pot reaction, DNA/DNA exchange is mediated by DOC washing of the original wrapping sequence, and ~ 50-times higher concentration of G-containing sequence over original wrapping DNA ($T_3C_3T_3C_6$) for the rewrapping process. We designed an experiment to demonstrate that DNA/DNA exchange indeed takes place under this condition. A clear red-shifted E_{11} peak can be observed after $T_3C_3T_3C_6$-(8,3) was replaced by GGCCGG (**Fig. S5**).

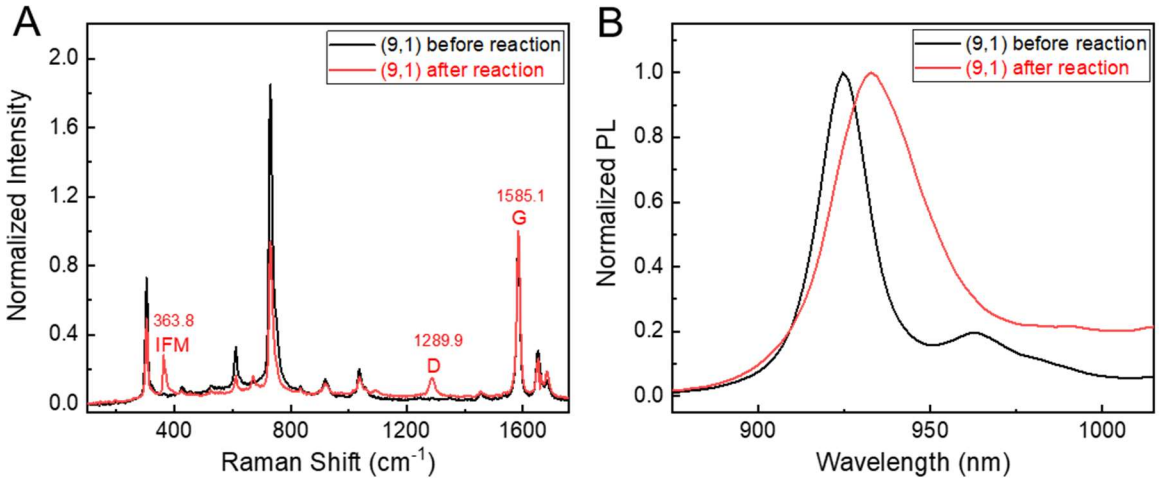

Fig. S6. Spectral characterization of (9,1) before and after reaction. (A) Raman spectra (normalized at the G peak); (B) Normalized PL spectra. The reactive G-containing sequence is $(GCGCCC)_6$. Spectra in A and B are measured with 671 nm excitation.

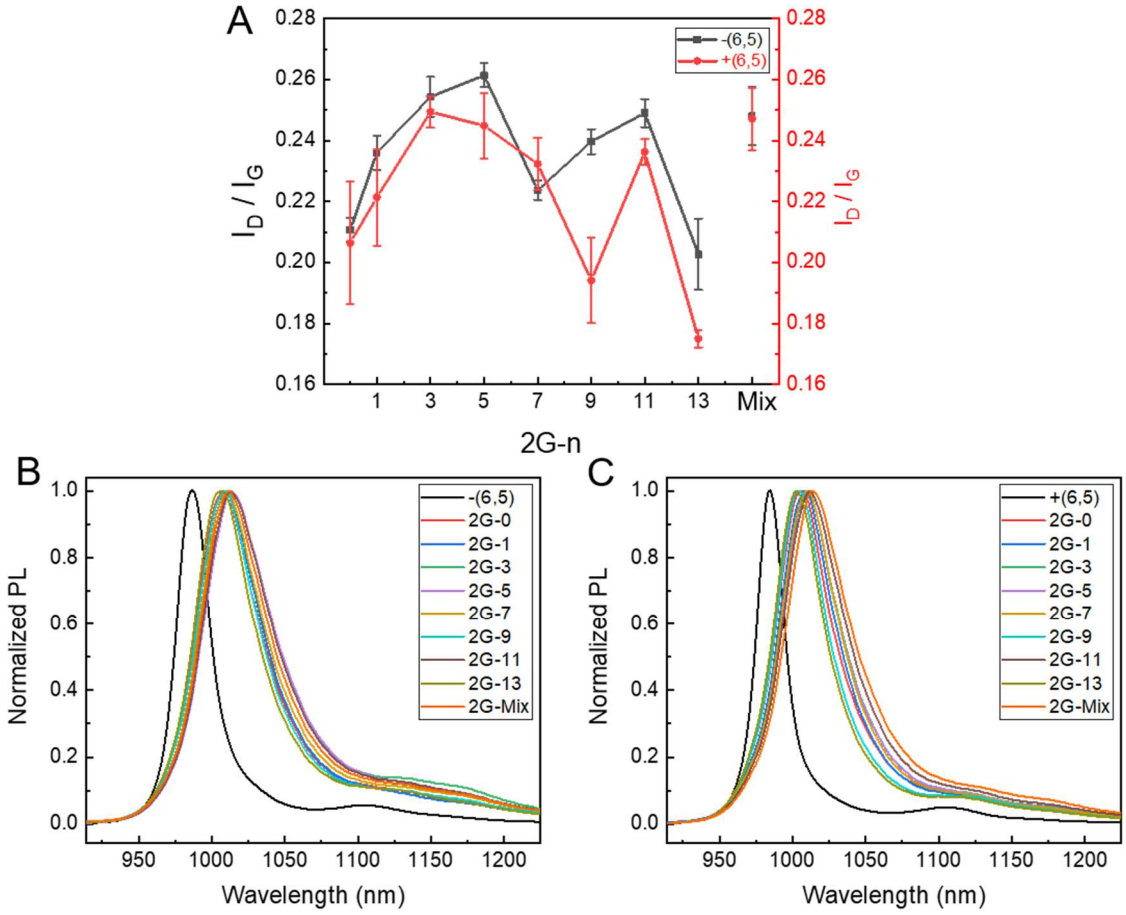

Fig. S7. Raman and PL spectroscopy characterization of ±(6,5) functionalized with sequences of 2G-n. (A) D peak intensity of ±(6,5) as a function of sequence pattern; (B) and (C) PL spectra of –(6,5) and +(6,5) as a function of sequence pattern. Spectra are measured with 532 nm excitation.

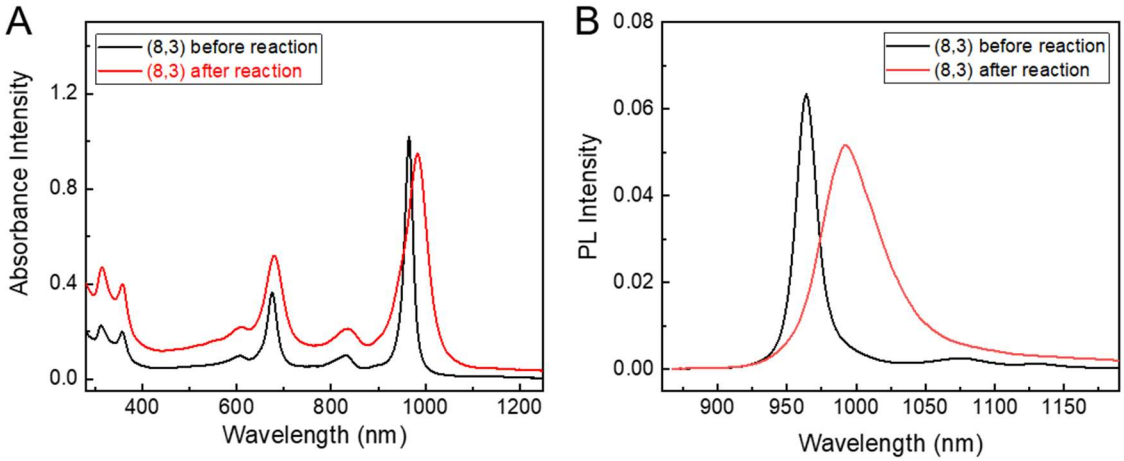

Fig. S8. Original data of (A) absorbance, (B) PL for **Fig. 1**. Spectra in B are measured with 671 nm excitation.

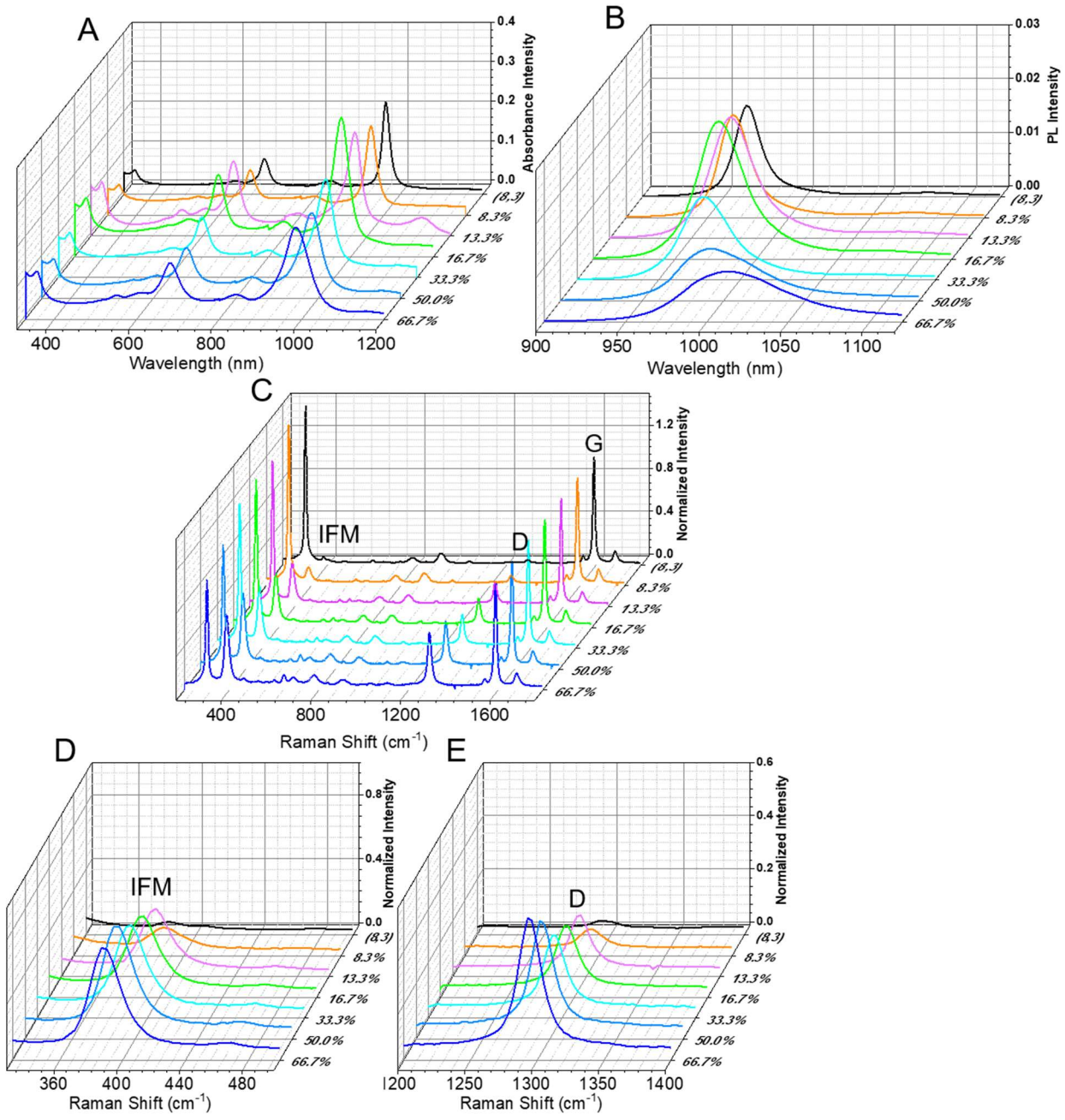

Fig. S9. Original data of (A) absorbance, (B) PL, (C, D, E) Raman spectra for **Fig. 2**. Spectra in B-D are measured with 671 nm excitation.

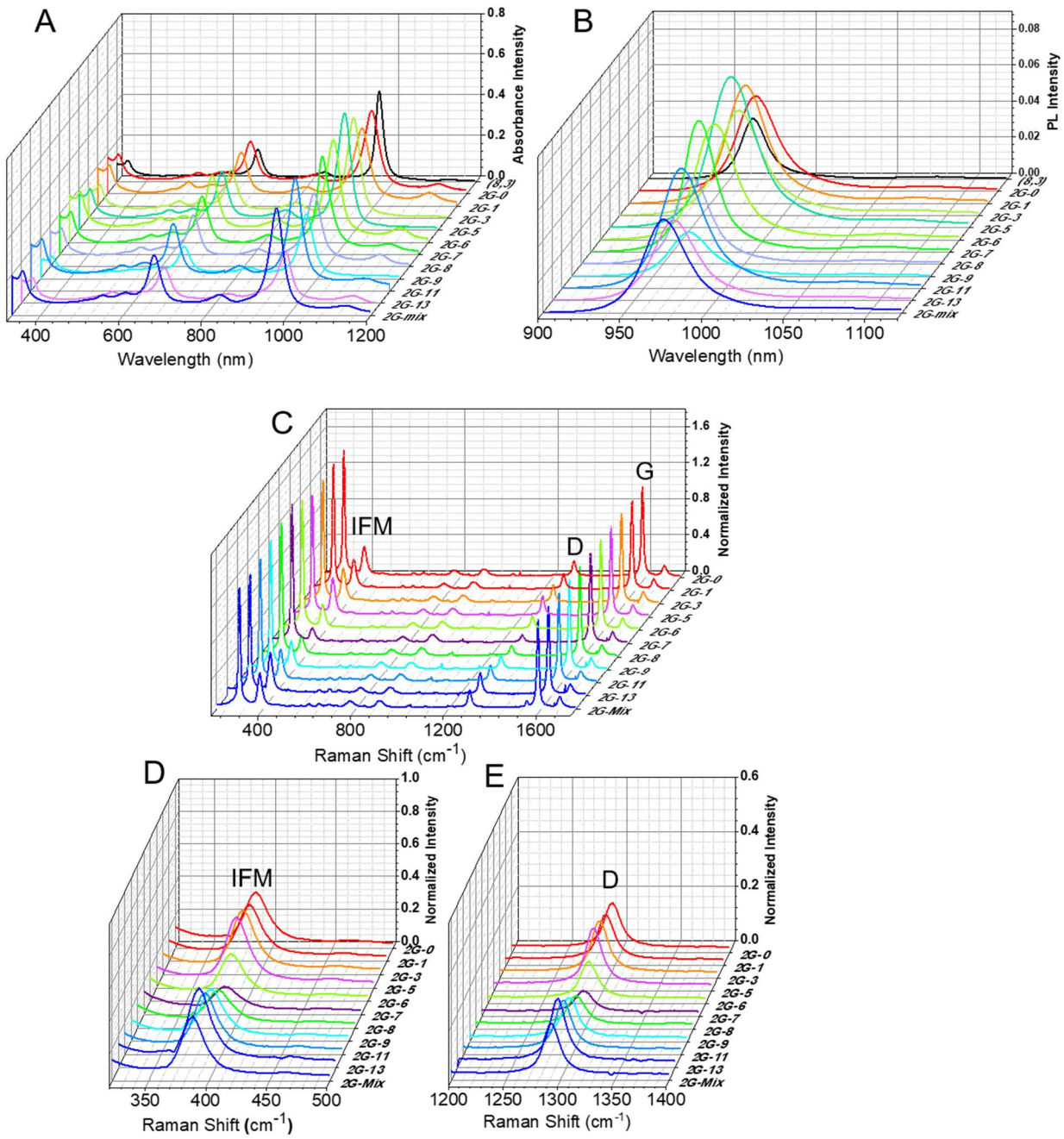

Fig. S10. Original data of (A) absorbance, (B) PL, (C, D, E) Raman spectra for **Fig. 3**. Spectra in B-D are measured with 671 nm excitation.

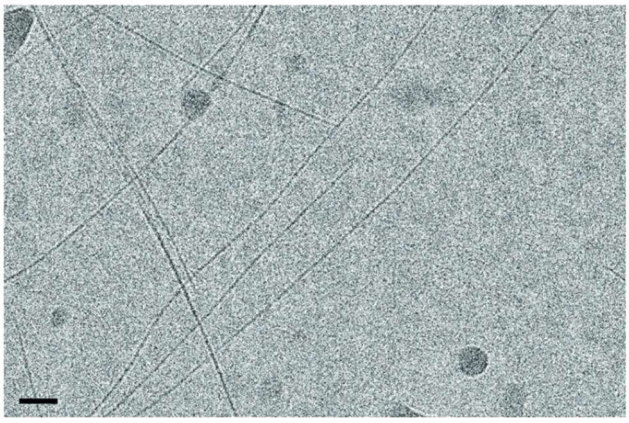

Fig. S11. A representative cryo-EM micrograph of 2G-7-functionalized (8,3). Scale bar 20 nm.

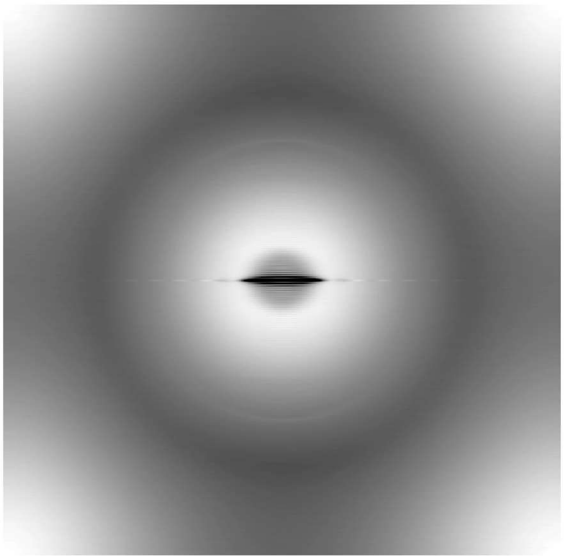

Fig. S12. Cryo-EM data of the control unfunctionalized 2G-7-(8,3). Averaged power spectrum of approximately 200000 particles, showing no periodicities.

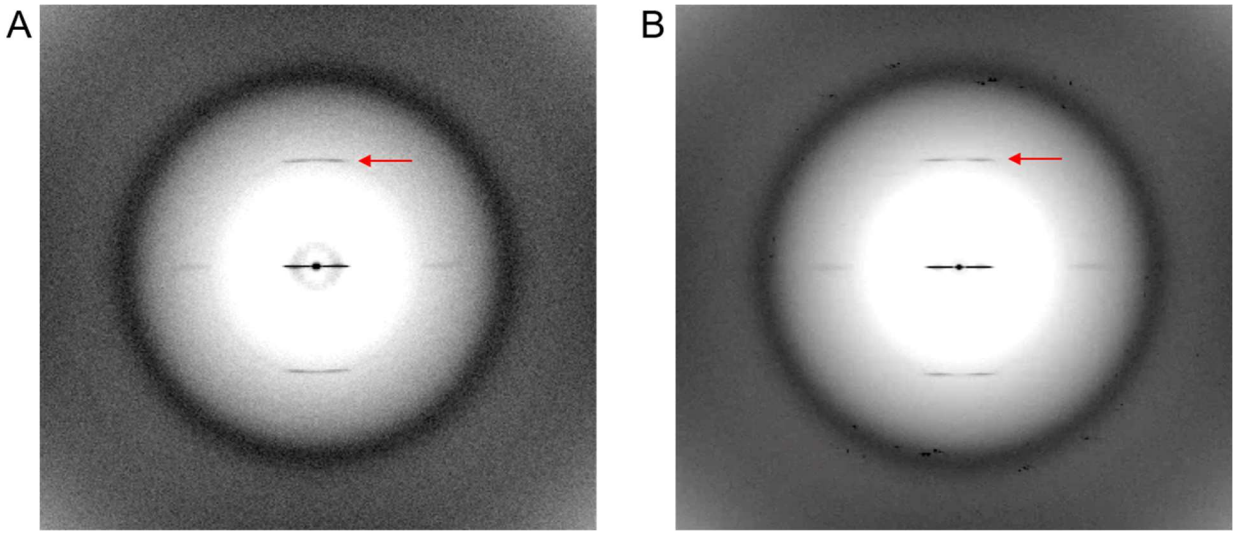

Fig. S13. (A) Averaged power spectrum of 2G-5-functionalized-(8,3); (B) Averaged power spectrum of 2G-6-functionlized-(8,3). Red arrow points to a layer line with a spacing of 1/(6.5 Å) from the equator.

Discussion on Fig. S13: The cryo-EM results in **Fig. S13** reinforce the reaction mechanism that G reacts with C-C bonds of maximum curvature to pin the DNA sequence on an armchair line. While cryo-EM detects the order of the overall wrapping structure, it does not have enough resolution to determine the location of Gs. Spectroscopy, on the other hand, is more specific to the order of covalent functionalization sites. It shows that 2G-7 has the smallest disorder (**Fig. 3**), which we interpret as due to all the G functionalized sites for this sequence being equally spaced along the armchair line.

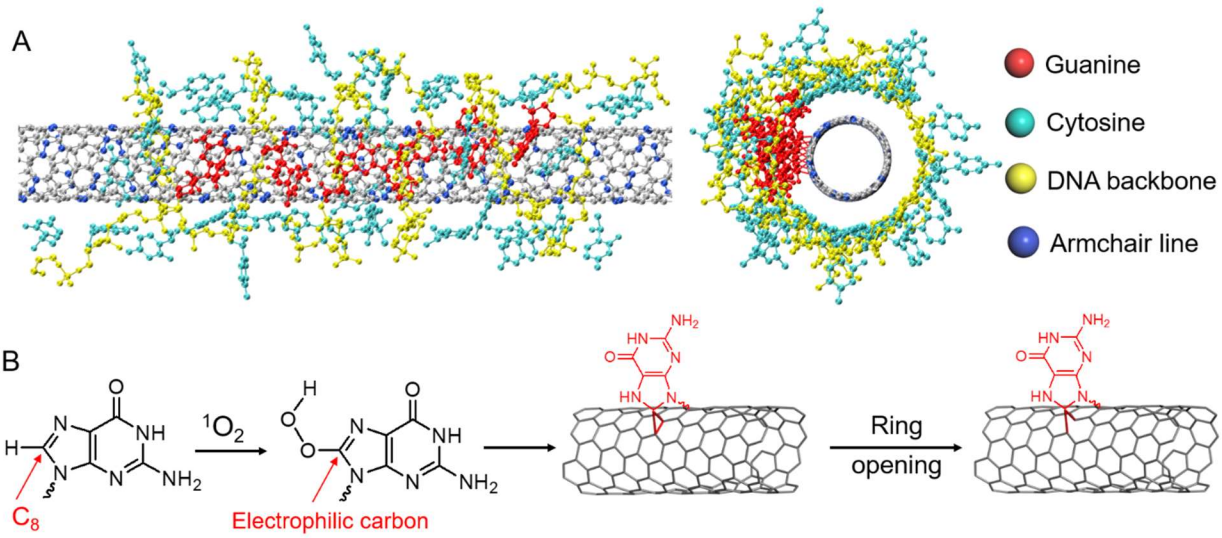

Fig. S14. (A) Modeling of 2G-7-functionalized (8,3), (B) A proposed reaction mechanism.

References

27. G. Ao, C. Y. Khripin, M. Zheng, DNA-Controlled Partition of Carbon Nanotubes in Polymer Aqueous Two-Phase Systems. *Journal of the American Chemical Society* **136**, 10383-10392 (2014).
28. G. Ao, J. K. Streit, J. A. Fagan, M. Zheng, Differentiating Left- and Right-Handed Carbon Nanotubes by DNA. *Journal of the American Chemical Society* **138**, 16677-16685 (2016).
29. Z. A. De los Santos, Z. Lin, M. Zheng, Optical Detection of Stereoselective Interactions with DNA-Wrapped Single-Wall Carbon Nanotubes. *Journal of the American Chemical Society* **143**, 20628-20632 (2021).
30. M. Lyu, B. Meany, J. Yang, Y. Li, M. Zheng, Toward Complete Resolution of DNA/Carbon Nanotube Hybrids by Aqueous Two-Phase Systems. *Journal of the American Chemical Society* **141**, 20177-20186 (2019).